Title

Sustained delivery and molecular targeting of a therapeutic monoclonal antibody to metastases in the central nervous system of mice

Journal

Nature Biomedical Engineering, 3(9)

ISSN

2157-846X

Authors

Wen, Jing

Wu, Di

Qin, Meng

et al.

Publication Date

2019-09-01

DOI

10.1038/s41551-019-0434-z

Peer reviewed

HHS Public Access

Author manuscript

Nat Biomed Eng. Author manuscript; available in PMC 2020 February 05.

Published in final edited form as:

Nat Biomed Eng. 2019 September ; 3(9): 706–716. doi:10.1038/s41551-019-0434-z.

Sustained delivery and molecular targeting of a therapeutic monoclonal antibody to metastases in the central nervous system of mice.

Jing Wen[1,2,&], **Di Wu**[3,&], **Meng Qin**[1,2], **Chaoyong Liu**[3], **Lan Wang**[1,2], **Duo Xu**[3], **Harry V. Vinters**[4], **Yang Liu**[5], **Emiko Kranz**[2,6], **Xin Guan**[7], **Guibo Sun**[8], **Xiaobo Sun**[8], **YooJin Lee**[1,2], **Otoniel Martinez-Maza**[1,2,10], **Daniel Widney**[2,9], **Yunfeng Lu**[3,*], **Irvin SY. Chen**[1,2,*], **Masakazu Kamata**[2,6,*]

[1]Department of Microbiology, Immunology and Molecular Genetics, David Geffen School of Medicine at University of California, Los Angeles (UCLA), Los Angeles, CA 90095, USA

[2]UCLA AIDS Institute, Los Angeles, CA 90095, USA

[3]Department of Chemical and Biomolecular Engineering, School of Engineering, UCLA, Los Angeles, CA 90095, USA

[4]Departments of Pathology & Laboratory Medicine (Neuropathology) and Neurology, David Geffen School of Medicine at UCLA, Los Angeles, CA 90095, USA

[5]State Key Laboratory of Medicinal Chemical Biology, Institute of Polymer Chemistry, College of Chemistry, Nankai University, Tianjin 300350, China

[6]Division of Haematology-Oncology, David Geffen School of Medicine at UCLA, Los Angeles, CA 90095, USA

[7]Biopharmaceutical R&D Center, Chinese Academy of Medical Sciences & Peking Union Medical College, Suzhou, China

[8]Institute of Medicinal Plant Development, Chinse Academy of Medical Sciences & Peking Union Medical College, Beijing 100193, China

[9]Department of Obstetrics & Gynecology, David Geffen School of Medicine at UCLA, Los Angeles, CA 90095, USA

[*]Corresponding authors, masa3k@ucla.edu; syuchen@mednet.ucla.edu; luucla@ucla.edu. **Correspondence and requests for materials** should be addressed to M.K.

[&]These authors contributed equally

Author contributions

J.W. and M.K.: contributed to the study design, performed the experiments, analyzed data, and wrote the paper. D.Wu, M.Q., C.L., L.W., D.X., H.V.V., Y.Liu, E.K., X.G, G.S., Y.Lee, and X.S.: performed the experiments. D.Widney, O.M.M, and Y.Lu.: interpreted data. I.S.Y.C: wrote the paper and interpreted data. All authors reviewed the manuscript.

Competing interests

I.S.Y.C has a financial interest in CSL Behring. The remaining authors declare no competing interests.

Additional information

Supplementary information is available for this paper at https://doi.org/10.1038/s41551-01X-XXXX-X.

Publisher's note: Springer Nature remains neutral with regard to jurisdictional claims in published maps and institutional affiliations.

[10]Department of Epidemiology, School of Public Health, UCLA, Los Angeles, CA 90095, USA

Abstract

Approximately 15–40% of all cancers develop metastases in the central nervous system (CNS), yet few therapeutic options exist to treat them. Cancer therapies based on monoclonal antibodies are widely successful, yet have limited efficacy against CNS metastases, owing to the low levels of the drug reaching the tumour site. Here, we show that the encapsulation of rituximab within a crosslinked zwitterionic polymer layer leads to the sustained release of rituximab as the crosslinkers are gradually hydrolyzed, enhancing by approximately 10-fold the CNS levels of the antibody with respect to the administration of naked rituximab. When the nanocapsules are functionalized with CXCL13, the ligand for the chemokine receptor CXCR5 frequently found on B-cell lymphoma, a single dose led to improved control of CXCR5-expressing metastases in a murine xenograft model of non-Hodgkin lymphoma, and eliminated lymphoma in a xenografted humanized bone-marrow–liver–thymus mouse model. Encapsulation and molecular targeting of therapeutic antibodies could become an option for the treatment of cancers with CNS metastases.

Treatments for cancer metastases, especially those of the central nervous system (CNS), are less successful than those for primary tumors [1]. Approximately 15%−40% of all cancers develop a CNS metastasis [2,3], which most commonly arises from lung cancer, melanoma, breast cancer, and colorectal cancer. Therapeutic monoclonal antibodies (mAbs) have revolutionized the treatment of cancer; however, their efficacy is limited in patients with CNS metastases due to insufficient mAb CNS delivery—typically 0.1% of the levels in plasma [4]. By bypassing the blood-brain barrier (BBB) through intrathecal or intraventricular administration, mAb therapy has shown some effectiveness against CNS tumor metastases [4–10]. However, direct CNS administration is invasive, with potential for neurotoxicity, and is limited by rapid efflux of antibodies from the CNS within hours [5,10,11]. Therefore, novel approaches for mAbs delivery are preferable to maintain systemic therapeutic effect in the CNS with improved efficiency.

To date, various carrier vehicles for macromolecule delivery such as viral vectors, liposomes, cationic polymers, inorganic delivery systems, and other biomolecules have been explored to improve CNS delivery [12–14]. Viral vectors are effective for CNS delivery in some settings but have potential safety concerns [15,16]. Liposome-based protein delivery has been shown to penetrate the BBB, but with relatively low efficiency, biocompatibility, and stability [17,18]. Polymer nanoparticles conjugated to target ligands with a variety of structures and morphologies have been used to form micelles through self-assembly, but *in vivo* instability, tissue-specific accumulations, and protein denaturation during complexing are problematic [19,20]. Inorganic delivery systems, including gold nanoparticles [21,22] and mesoporous silica particles [23], are non-biodegradable and difficult to load or conjugate with macromolecules. Biomolecules, such as cell-penetrating peptides and antibodies, have improved the efficacy of macromolecule delivery, but degradation of cargo still hampers their therapeutic applications [24]. The above approaches have shown promise, but drastic improvements are needed—especially in the systemic delivery of macromolecules into the CNS [19,25].

Rituximab (RTX) for treatment of non-Hodgkin lymphoma (NHL) was the first anti-cancer antibody approved by the U.S. Food and Drug Administration. RTX binds to CD20+ lymphoma cells and induces cell death through complement-dependent cytotoxicity (CDC), antibody-dependent cell-mediated cytotoxicity (ADCC), and apoptosis [26]. RTX may also promote anti-lymphoma immune responses [27]. The substantial benefits of RTX administration in treatments for systemic NHL are well-established, but treatment of primary and relapsed CNS lymphoma has not been effective through the intravenous route, likely due to the very low levels of systemic RTX entering the CNS [4]. CNS involvement in NHL is relatively rare, but there is elevated risk in patients with immunodeficiency diseases [9] or renal, cardiac, lung, and liver transplants.

We demonstrate that compared to administration of native RTX, timed-release nanocapsule delivery of RTX achieves levels around 10-fold higher RTX concentration in the CNS following a single-course treatment and is maintained for at least 4 weeks, as opposed to 1 week with native RTX. Furthermore, we developed a human NHL xenograft murine model for CNS metastases and show therapeutic efficacy of RTX nanocapsules against CNS lymphomas. In addition, using a humanized BLT mouse model, we demonstrate clearance of CNS lymphomas.

Results and discussion

Nanocapsules facilitate CNS penetration

We have developed a nanotechnology strategy whereby individual macromolecules are encapsulated within a thin polymer shell formed by *in situ* polymerization of monomers and stabilized by environmentally-responsive crosslinkers [28,29]. Like a virion capsid, the polymer shell shields cargo from the environment and confers high resistance to denaturation, proteases, and nucleases, and determines the distribution of nanocapsules. Nanocapsules with polymer shells formed by neutral monomers with zwitterionic properties, 2-methacryloyloxyethyl phosphorylcholine (MPC), exhibited broad biodistribution [30] and a long half-life [31]. MPC is used in contact lenses and tested for use in coronary stents and other medical devices [32,33] and is inert, highly stable, resistant to protein adsorption, and lacks immunogenicity. We synthesized RTX nanocapsules with MPC monomers and glycerol dimethacrylate (GDMA) crosslinkers, which are efficiently degraded under acidic conditions but deteriorate very slowly under physiological conditions (termed n-$RTX_{(GDMA)}$).

We first evaluated the biodistribution and brain delivery efficiency of our nanoparticles without release of the RTX cargo under physiologic conditions using n-$RTX_{(GDMA)}$ (Supplementary Fig.1). Biodistribution of the nanocapsules was assayed by enzyme-linked immunosorbent assay (ELISA) after releasing RTX by acid treatment (pH5.4) at 4 ^{O}C for overnight *ex vivo*. Higher levels of n-$RTX_{(GDMA)}$ were present in plasma by day 7. Importantly, more RTX released from n-$RTX_{(GDMA)}$ was observed in the brain and cerebrospinal fluid (CSF). Levels of released RTX in CSF were 1.7–5.5% the levels in plasma (5.5% on day 1, 1.7 % on day 7, and 3% on day21); native RTX was undetectable in CSF at all three points. This is consistent with the relative inability of antibodies to cross the BBB [4].

To achieve proper release of mAb for therapeutic treatment, nanocapsules were designed to release cargo over time. This is accomplished by securing the polymer shell with mixed crosslinkers that are hydrolyzed gradually under physiological conditions (Fig.1A). MPC monomers are enriched around the surface of individual RTX molecules through electrostatic interactions, then hydrolysable crosslinker (Poly(DL-lactide)-b-Poly(ethylene glycol)-b-Poly(DL-lactide)-diacrylate triblock copolymers (PLA-PEG-PLA) and slowly-hydrolysable crosslinker GDMA are associated by hydrogen bonding under physiological conditions. Subsequent polymerization in an aqueous solution wraps each molecule with a thin shell of polymer through *in-situ* free-radical polymerization. When PLA-PEG-PLA is hydrolyzed by body fluids, the nanocapsules dissociate and release encapsulated RTX. These nanocapsules have a relatively uniform, small diameter of 20–30 nm as measured by transmission electron microscope (TEM) (Supplementary Fig.2) and consist of a single-RTX molecule core-shell structure (Supplementary Fig.3). To sustain timed release in plasma at neutral pH, we mixed GDMA with PLA-PEG-PLA to achieve different release rates. Depending on the relative ratios of PLA-PEG-PLA (100%, 50%, 30%, and 10%), these nanocapsules released RTX at different rates under physiological conditions (Fig.1B): RTX nanocapsules with 50% PLA-PEG-PLA crosslinker (termed n-RTX) enabled gradual release over 7 days. Importantly, lower pH (pH 5.5–6.0) allowed accelerated RTX release (Fig.1C), which would facilitate quicker release of RTX in the lower pH tumor microenvironment [34,35] than in the bloodstream or healthy tissues.

We next examined the kinetics of RTX released from nanocapsules with 50% PLA-PEG-PLA crosslinker in B6 mice (Fig.1D,E). Mice were injected with a single intravenous dose of either n-RTX or native RTX. Except for Day 1, where RTX was slightly lower in the n-RTX group, there were comparable levels in plasma through Day 28. In contrast, 8 to 10-fold enhancements of free RTX levels were observed in the CNS and brain tissue when delivered by n-RTX relative to native RTX. Mice treated with n-RTX had detectable levels of RTX in the CNS and brain for up to 4 weeks. Similar results were also confirmed in rats (data not shown). Immunohistochemical staining of rat brains treated with n-RTX showed normal microglia and astrocyte morphology (Supplementary Fig.4) [36,37]. No significant elevation of ionized calcium-binding adapter molecule 1 (Iba1) in microglial cells nor glial fibrillary acidic proteins (GFAP) in astrocytes of rat brains treated with nanocapsules were observed compared to untreated control animals (Supplementary Fig.4B,C). These results provide proof of concept for penetration, release, maintenance, and safety of mAb nanocapsules in both plasma and CNS.

Encapsulated RTX effectively controls CNS lymphoma formation

Next, we compared anti-lymphoma efficacy of native RTX and n-RTX in a xenograft murine model. We first established a human NHL xenograft murine model that can consistently form CNS lymphomas with 2F7 cells, a cell line derived from AIDS-associated B-cell NHL [38]. These 2F7 cells were marked with an mStrawberry reporter gene by a lentiviral vector. Individual sub-clones were tested for their ability to metastasize into the CNS. Two out of ten sub-lines formed CNS lymphomas within 7 weeks after intraperitoneal injection. Lymphoma cells were isolated from the brain of one of these sub-lines and re-adapted to cell culture. The resulting cell line, termed “2F7-BR44,” forms CNS lymphomas in 100% of

mice within 7 weeks following intraperitoneal injection (Supplementary Fig.5A) or 1–2 weeks following tail vein injection of 2×10^6 cells (Supplementary Fig.5B). 2F7-BR44 cells maintain expression of four pan-B cell markers (CD19, CD20, CD22, and CXCR5) at levels comparable to the parental 2F7 cells (Supplementary Fig.6A). The cells are sensitive to apoptosis mediated by RTX, comparable to the parental cell line, and also sensitive to complement *in vitro* (Supplementary Fig.6B,C).

Lymphoma burden and therapeutic efficacy were quantified by evaluating the percentage of mStrawberry+ 2F7-BR44 cells in different tissues. CNS metastases generally arise later than those in systemic organs; without treatment, animals usually die from systemic complications. Mice with lymphoma show apparent signs of lymphoma burden such as weight loss, pale skin, anemia, and decreased activity. Once the lymphoma burden in CNS increases up to ~15%, as quantified by the percentage of mStrawberry+ in single cell fraction obtained from whole brain tissues following perfusion, mice show hind leg paralysis. Native RTX treatment significantly extended survival of mice engrafted with 2F7-BR44 cells (Supplementary Fig.7B) and efficiently reduced lymphoma burden in bone marrow as well as to a lesser extent in spleen, but was ineffective in brain as well as lymph nodes (Supplementary Fig.7C).

We next compared the efficacy of native RTX versus n-RTX in controlling lymphoma formation in the brain. n-RTX improved the therapeutic efficacy of RTX against CNS metastases in the NHL murine model; in contrast, untreated animals required euthanization at week 3.5–4 due to severe anemia (Fig.2A). Treatment significantly improved mouse life span: native RTX-treated mice survived up to week 5, whereas half of the n-RTX-treated mice showed no symptoms of lymphoma formation in brain until the end time points (week 5.5). Both native RTX and n-RTX capably suppressed lymphoma formation in bone marrow. In contrast, n-RTX significantly reduced lymphoma burden in the brain, whereas native RTX had no effect despite effective systemic control (Fig.2B). The correlation between controlled lymphoma growth and heightened RTX concentration illustrated by these results further demonstrates that RTX delivered via nanocapsules exerts control over CNS metastases.

Nanocapsules conjugated with CXCL13 can target lymphoma cells by binding to CXCR5

Ligands can be readily conjugated to the surface of nanocapsules to redirect them to specific targets; thus, targeting nanocapsules to lymphoma cells is predicted to increase RTX concentrations at the site of the lymphoma, enhancing potency and specificity of activity. To demonstrate the potential of ligand-mediated lymphoma targeting, we selected CXCL13: a chemokine belonging to the CXC family that interacts with CXCR5, a receptor expressed on mature B cells [39,40], and is associated with NHLs of B cell origin [41–43]. In malignancies, CXCL13 has suspected involvement in metastasis of lymphoma cells [44,45]; therefore, to assure accurate modelling of the metastatic environment, we evaluated CXCR5 expression in 2F7-BR44 cells and confirmed that they showed a similar level of CXCR5 expression to that of parental 2F7 cells (Supplementary Fig.6A). We then conjugated CXCL13 to the surface of nanocapsules at a molar ratio of approximately 1:1 (Supplementary Fig.8, n-RTX^{CXCL13}). This conjugation did not induce significant change on either particle size or surface charge of n-RTX (Supplementary Fig.9A,B).

To evaluate the binding of CXCL13-conjugated nanocapsules, EGFP was used as a model protein for nanocapsule synthesis with GDMA crosslinkers which are slowly hydrolysable under physiological conditions (n-$EGFP_{(GDMA)}$ and n-$EGFP_{(GDMA)}^{CXCL13}$). We found that CXCL13 conjugation improved the specific binding of nanocapsules on 2F7-BR44 cells (Fig.3B, 2F7) while minimizing non-specific binding on non-targeted cells (Fig.3B, Jurkat); this specific binding of n-$EGFP_{(GDMA)}^{CXCL13}$ on 2F7-BR44 cells was further confirmed by flow cytometry (Fig.3C). Importantly, CXCL13 conjugation did not change the surface properties of MPC nanocapsules, maintaining resistance to cellular uptake. Similarly to n-$RTX_{(GDMA)}$, n-$RTX_{(GDMA)}^{CXCL13}$ bound to 2F7-BR44 cells but was not internalized (Supplementary Fig.10). Biodistribution data showed that both n-$RTX_{(GDMA)}$ and n-$RTX_{(GDMA)}^{CXCL13}$ systemically distributed in mice (Fig.3D), were delivered with uniform efficiency within the brain, and exhibited decreased accumulation in the liver, kidney, and lung—tissues known for showing non-specific accumulation of antibody (Fig.3E,F).

We next demonstrated the enhanced effectiveness of n-RTX conjugated with CXCL13 (n-RTX^{CXCL13}) in controlling lymphoma growth in a xenograft murine model. Compared to native RTX, there was significant improvement in the kinetics of RTX delivery released from both n-RTX and n-RTX^{CXCL13} into CSF and brain; minimal differences were noted between the two kinds of nanocapsules (Supplementary Fig.11A). Moreover, there were no clear liver or kidney toxicities over 4 weeks of nanocapsule treatment (Supplementary Fig. 11B). Importantly, compared to native RTX and n-RTX-treated animals, mice treated with n-RTX^{CXCL13} showed improved survival rate (Fig.4A) and minimal CNS lymphoma formation until the end time points (Fig.4B). Greater amounts of n-RTX^{CXCL13} were observed in areas of lymphoma growth (Fig.4C,D), indicating that n-RTX^{CXCL13} preferentially locates with 2F7-BR44 lymphoma in the brain. Besides lymphomas in brain, renal lymphoma and intraocular lymphoma were also observed in this NHL murine model. Unlike native RTX treatment, intraocular lymphoma was prevented by treatment with n-RTX; however, nodules still formed on kidneys (Fig.4E). n-RTX^{CXCL13} showed clear colocalization with 2F7-BR44 cells in the kidney (Supplementary Fig.12) and exerted superior anti-lymphoma activity in both locations compared to native RTX or n-RTX (Fig. 4E).

Nanocapsules conjugated with CXCL13 improved therapeutic efficacy at different stages of lymphoma progression

To facilitate longitudinal analysis of lymphoma location and progression, the NHL mouse model was further adapted for optical imaging by marking 2F7-BR44 cells with a lentiviral vector expressing firefly luciferase (2F7-BR44-Luc). Following injection of D-luciferin, the substrate of luciferase, *in vivo* distributions and growth of 2F7-BR44-Luc cells were monitored by *in vivo* bioluminescence imaging over time (Supplementary Fig.13). Bioluminescence imaging in the NHL xenograft murine model indicated that 2F7-BR44 cells initially migrated into the lungs after tail vein injection, followed by redistribution to CNS (brain and spinal cord) and bone marrow (BM) from sternum and femur within the first week. At week 2, signal intensity from lymphomas in the brain, spinal cord, sternum, femur, and kidneys increased.

Based upon the kinetics of lymphoma formation, we conducted studies in which treatment was initiated after lymphoma formation. Mice were treated with native RTX or n-RTX^{CXCL13} at different times: week 1 (Group I) and week 2 (Group II) post-injection of 2F7-BR44-Luc cells. Treatment by n-RTX^{CXCL13} in both groups resulted in significant control of lymphoma burden relative to native RTX treatment, measured by bioluminescence per a defined area (Fig.5A,B). Survival of lymphoma-bearing mice was significantly extended by 1–2 weeks via n-RTX^{CXCL13} treatment compared to native RTX treatment in both Group I and II (Fig.5C,D). To quantify the difference in therapeutic efficacy between native RTX and n-RTX^{CXCL13}, bioluminescence intensity (BLI) from 2F7-BR44-Luc cells in the whole body was compared every week after treatment (Fig.5E,F). In Group I, whole body therapeutic efficacy was similar in the first week post-treatment across both treatment types but was significantly improved by n-RTX^{CXCL13} later, suggesting more effective control of lymphoma burden by n-RTX^{CXCL13}. In Group II, there was a significantly greater effect of n-RTX^{CXCL13} treatment, but less than in mice treated in Group I. To assess the impact upon CNS lymphomas, BLIs from the head area were quantified (Fig.5G,H). Treatment with n-RTX^{CXCL13} notably slowed and controlled CNS lymphoma burden in both groups. In Group II, where lymphomas had already formed in CNS before treatment, all mice with n-RTX^{CXCL13} showed a decrease in lymphoma burden at 1 week following treatment.

Nanocapsules conjugated with CXCL13 eliminated lymphoma in xenograft humanized BLT mice

The above NHL xenograft murine model uses immunodeficient mice in which the killing of 2F7-BR44-Luc cells is likely to be primarily, if not exclusively, by induction of apoptosis. RTX is known to induce anti-lymphoma killing through multiple mechanisms in addition to apoptosis, including ADCC and CDC [26]. Thus, the efficacy of RTX against CNS lymphomas in the NHL xenograft model is highly limited [46]. We further evaluated n-RTX^{CXCL13} in a humanized BLT (bone marrow/liver/thymus) murine model wherein human T cells, B cells, natural killer (NK) cells, and macrophages reconstitute; of these populations, both NK cells and macrophages can induce ADCC. Humanized BLT mice develop notably human NK and macrophage populations in tissues, including the brain [47–50]. Consistent with a published study [51], we found substantial macrophage repopulation in the brains of these mice (data not shown). Humanized BLT mice were treated with native RTX or n-RTX^{CXCL13} at week 1 post-injection of 2F7-BR44-Luc cells and monitored for lymphoma growth for 12 weeks while unrelated antibody Herceptin (anti-human epidermal growth factor receptor (HER) 2) and n-HER^{CXCL13} were included as negative controls. Native RTX treatment showed effective therapeutic efficacy throughout the body except in brain, which resulted in paralysis on weeks 4–8; additionally, neither native HER nor n-HER^{CXCL13} treatment showed any therapeutic effect (Fig.6A). In contrast, n-RTX^{CXCL13} completely eliminated lymphomas in mice and initiated regression of CNS lymphomas, with no relapse observed even until the endpoint at week 13. Survival of lymphoma-bearing mice was significantly extended by n-RTX^{CXCL13} treatment (Fig.6B). The clearance of lymphomas was confirmed by flow cytometry of tissues (Fig.6C).

We demonstrate that a single-course treatment of RTX encapsulated within an MPC-based nanocapsule designed to administer mAb by timed release results in CNS RTX concentrations up to 10-fold higher than native antibody and yields detectable levels for at least 4 weeks in a murine model. Using an NHL xenograft murine model, better penetration into the CNS allows control of CNS lymphoma formation. Three basic components were tuned to increase anti-lymphoma effects of RTX: 1) a polymer shell which allows longer systemic circulation and CNS penetration, 2) crosslinkers which stabilize the polymer shell and release mAb through timed hydrolysis, and 3) CXCL13 conjugated to the surface enabling targeting to CXCR5-expressing lymphoma cells. CNS penetration of the nanocapsules appears to be mediated by binding of choline and acetylcholine analogues of the nanocapsule polymer shell to choline transporters and acetylcholine receptors [52].

Enhanced RTX levels in the CNS could act to control local lymphoma growth through various effector mechanisms. Both CDC and ADCC function in the CNS [53–56], but are likely limited due to low antibody levels. In the NSG xenograft murine model, induction of apoptosis is likely to be the major mechanism for lymphoma cell elimination since complement components are absent; it is unclear whether murine microglia may contribute to ADCC activity [54]. With limited effector functions, only partial control was achieved in xenografted NSG mice. By repeating studies in humanized BLT mice wherein human macrophages and NK cells differentiate, we demonstrated complete elimination of lymphomas both systemically and in the CNS. We suspect that the differences between these two murine models exist due to the presence of ADCC in the humanized BLT mice, which is absent in the standard xenograft model using NSG mice. Future studies will better elucidate the mechanisms responsible for lymphoma control and clearance.

Outlook

The strategy described here should be applicable to other therapeutic mAbs wherein CNS penetration is limited. For example, breast cancer patients under systemic Herceptin therapy often relapse with CNS metastases that are resistant to mAb therapy [7,57]. By bypassing the BBB through intrathecal or intraventricular administration, mAb therapy for lymphoma and breast cancer has shown some effectiveness against CNS metastases [7,58]. Our results suggest a potential non-invasive alternative treatment of CNS lymphomas as well as a potential prophylactic use of the nanocapsules against CNS metastases. Since the biodistribution of the mAb is conferred by the nanocapsules, not the cargo, any mAb (or protein) could be used. Anti-phosphorylcholine autoantibodies have been reported in mice [59] and humans [60], and could potentially affect the *in vivo* dynamics of nanocapsules generated with MPC, though we do not observe more rapid clearance relative to native mAb. We anticipate that further studies on the biodistribution and optimization of formulations through the engineering of polymers, crosslinkers and targeting ligands will further improve CNS delivery and therapeutic efficacy for CNS diseases.

Methods

Synthesis of nanocapsules

Nanocapsules were synthesized with optimized modification for antibodies based on our previous reports[31]. Proteins (RTX or EGFP) were encapsulated via *in situ* polymerization at room temperature using MPC as the monomer, PLA-PEG-PLA and/or GDMA as the crosslinker, and ammonium persulfate and tetramethylethylenediamine as the initiator. Synthesized nanocapsules were dialyzed against PBS and purified by passing through a hydrophobic interaction column (Phenyl-Sepharose 4BCL). Detailed parameters, procedures, and characterization of the synthesis are provided in the Supplementary section.

Biodistribution studies

Biodistribution of native RTX and n-RTX was determined by monitoring the free RTX concentration in animal body fluids and perfused tissue homogenates. Briefly, C57BL/6 mice were randomly divided into two groups and retro-orbitally injected at a dosage of 20 mg/kg/mouse, a dose which has been reported as effective in an NHL xenograft murine model[61]. CSF was collected from a mouse under anesthesia by Ketamine and Xylazine (100 mg/kg each). After CSF collection, this mouse was perfused with cold phosphate-buffered saline (PBS), euthanized, and organs were harvested. All perfused tissues were homogenized by vortexing with ceramic beads in PBS containing protease inhibitor cocktail.

Non-Hodgkin Lymphoma (NHL) mouse model with CNS metastases

Animal research described in the study was approved by the University of California, Los Angeles (UCLA)'s Chancellor's Animal Research Committee (Institutional Animal Care and Use Committee [IACUC]), and was conducted in accordance with guidelines for housing and care of laboratory animals of the National Institutes of Health (NIH) and the Association for the Assessment and Accreditation of Laboratory Animal Care (AALAC) International. 2F7 cells were first marked with a fluorescent reporter gene by a lentiviral vector expressing mStrawberry. The 2F7 cells were then sub-cloned and tested individually for ability to metastasize into CNS. We selected clone 44 out of 10 clones, which showed stable brain metastatic ability. An NSG mouse received 2×10^6 mStrawberry+ 2F7 clone 44 cells via intraperitoneal injection and showed brain metastasis 7 weeks post-injection (see Supplementary Fig.5A). Lymphoma cells were isolated from the brain metastatic site and adapted to cell culture to establish the 2F7-BR44 cell line. 2×10^6 of 2F7-BR44 cells were injected into NSG mice via lateral tail vein to establish an NHL xenograft murine model with CNS metastases.

MAb detection by ELISA

The concentration of RTX in animal body fluids (CSF and plasma) and tissue homogenates was measured by ELISA against RTX. 96-well plates were coated with 1 μg/mL of anti-RTX antibody (diluted in sodium carbonate–bicarbonate buffer), followed by blocking with 1% BSA/PBS for 2 hours at room temperature. Diluted RTX in PBST (0.1% Tween/PBS) from 0 to 500 ng/mL were then added and incubated for an hour at room temperature to obtain calibration curves. Animal body fluids and tissue homogenates containing

encapsulated RTX in non-degradable nanocapsules were treated with 100 mM sodium acetate buffer (pH 5.4) at 4ºC overnight, then used for ELISA measurement. Free RTX released from n-RTX was directly measured with animal body fluids and tissue homogenates. All animal samples were added to the well and incubated for an hour at room temperature. After five-times wash with PBST, peroxidase-conjugated anti-human Fc antibody was added and incubated for an additional hour at room temperature. The substrate 3,3′,5,5′-Tetramethylbenzidine (TMB) solution was added and incubated until the appropriate color had developed. The reaction was stopped and absorbance at 450 nm was measured with a microplate reader.

Anti-lymphoma efficacy of RTX in the NHL xenograft murine model with CNS metastases

2F7-BR44 cells (2×10^6/animal) were injected into NSG mice via tail vein. Five days after 2F7-BR44 cell injection unless otherwise stated, mice were treated with a single course of native RTX, n-RTX, or n-RTX conjugated with CXCL13 (n-RTX^{CXCL13}) via retro-orbital vein injection (4mg/kg/day for 5 days). Mice were sacrificed when in critical condition due to lymphoma burden or at the end time points decided in experiment design. The mice were perfused with cold PBS, euthanized, and organs were harvested for single-cell isolation from tissues. Cells from target tissues were stained with anti-human CD45 and CD19, then analyzed by flow cytometry.

In vivo imaging to monitor lymphoma progression

2F7-BR44 cells were gene marked with a lentiviral vector expressing firefly luciferase, then luciferase-expressing cells were selected by a week of Zeocin treatment (200 μg/ml) (2F7-BR44-Luc). 2F7-BR44-Luc cells (2×10^6/animal) were injected into NSG mice or BLT humanized mice via tail vein. Humanized mice were prepared as previously described with modifications [62–64]. Human fetal tissue was purchased from Advanced Biosciences Resources (Alameda, CA) without identifying information, which did not require Institutional Review Board approval for its use. Six-week-old NSG mice were administered Busulfan (35 mg/kg) intraperitoneally. Twenty-four hours later, the mice were implanted with a portion of human fetal thymus combined with fetal liver-derived CD34+ cells solidified in Matrigel under the kidney capsule and also via retro-orbital vein injection. After the human blood cell reconstitution in peripheral blood, 2F7-BR44 cells (2×10^6/animal) were injected into humanized BLT mice via tail vein to establish xenograft humanized BLT mice. Lymphoma formation was monitored by *in vivo* bioimaging using the IVIS Lumina II in vivo imaging system (PerkinElmer, Waltham, MA). *In vivo* bioluminescence imaging was performed following subcutaneous injection of 4.5 mg D-luciferin (Pierce, Woodland Hills, CA). Mice were imaged at the signal plateau (10 minutes post-D-luciferin injection) under isoflurane anesthesia. Lymphoma burden was quantified as the total photon flux per second within a region of interest (ROI) (whole body or head area) of the mouse; ROIs were identically sized for all measurements. Sensitivity settings were adjusted at each time point to maintain 250–5000 counts per pixel for humanized mice and 500–5000 counts per pixel for NSG mice.

Statistical analyses

Results are expressed as mean ± standard deviations (SDs). Statistical significance is presented with a *p*-value calculated via GraphPad Prism. The significance of survival-curve data was compared with a log-rank test. All other significance comparisons between groups were calculated by one-tailed unpaired *t*-test with Welch's correction.

Reporting summary

Further information on research design is available in the Nature Research Reporting Summary linked to this article.

Data availability

The authors declare that all data supporting the results in this study are available within the paper and its Supplementary Information. Source data collected in this study are available from the corresponding author upon request.

Supplementary Material

Refer to Web version on PubMed Central for supplementary material.

Acknowledgements

This work was supported by the UCLA AIDS Institute HIV extinction project funded from the McCarthy Family Foundation (M.K.), NIH grants RO1 CA232015 and RO1 AI110200 (M.K.), U19AI117941 (I.S.Y.C) and R21 AI114433 (I.S.Y.C), and the California HIV/AIDS Research Grants Program (ID15-LA-050 to D.Widney). Equipment located in the UCLA AIDS Institute is supported by the James B Pendleton Charitable Trust. Cell sorting was performed in the CFAR Flow Cytometry Core Facility supported by NIH grants P30 CA016042 and 5P30 AI028697.

References

1. Chambers AF, Groom AC & MacDonald IC Dissemination and growth of cancer cells in metastatic sites. Nat Rev Cancer 2, 563–572 (2002). [PubMed: 12154349]
2. Aragon-Ching JB & Zujewski JA CNS metastasis: an old problem in a new guise. Clin Cancer Res 13, 1644–1647 (2007). [PubMed: 17363516]
3. Tosoni A, Ermani M & Brandes AA The pathogenesis and treatment of brain metastases: a comprehensive review. Crit Rev Oncol Hematol 52, 199–215 (2004). [PubMed: 15582786]
4. Rubenstein JL, et al. Rituximab therapy for CNS lymphomas: targeting the leptomeningeal compartment. Blood 101, 466–468 (2003). [PubMed: 12393404]
5. Zhang Y & Pardridge WM Mediated efflux of IgG molecules from brain to blood across the blood-brain barrier. J Neuroimmunol 114, 168–172 (2001). [PubMed: 11240028]
6. Czyzewski K, et al. Intrathecal therapy with rituximab in central nervous system involvement of post-transplant lymphoproliferative disorder. Leuk Lymphoma 54, 503–506 (2013). [PubMed: 22873830]
7. Lu NT, et al. Intrathecal trastuzumab: immunotherapy improves the prognosis of leptomeningeal metastases in HER-2+ breast cancer patient. J Immunother Cancer 3, 41 (2015). [PubMed: 26380087]
8. Cooper PR, et al. Efflux of monoclonal antibodies from rat brain by neonatal Fc receptor, FcRn. Brain Res 1534, 13–21 (2013). [PubMed: 23978455]
9. Rubenstein JL, et al. Multicenter phase 1 trial of intraventricular immunochemotherapy in recurrent CNS lymphoma. Blood 121, 745–751 (2013). [PubMed: 23197589]

10. Rubenstein JL, et al. Phase I study of intraventricular administration of rituximab in patients with recurrent CNS and intraocular lymphoma. J Clin Oncol 25, 1350–1356 (2007). [PubMed: 17312328]
11. Bousquet G, et al. Intrathecal Trastuzumab Halts Progression of CNS Metastases in Breast Cancer. J Clin Oncol 34, e151–155 (2016). [PubMed: 25547506]
12. Chen Y & Liu L Modern methods for delivery of drugs across the blood-brain barrier. Adv Drug Deliv Rev 64, 640–665 (2012). [PubMed: 22154620]
13. Schroeder A, et al. Treating metastatic cancer with nanotechnology. Nat Rev Cancer 12, 39–50 (2011). [PubMed: 22193407]
14. Lu CT, et al. Current approaches to enhance CNS delivery of drugs across the brain barriers. Int J Nanomedicine 9, 2241–2257 (2014). [PubMed: 24872687]
15. Fu H & McCarty DM Crossing the blood-brain-barrier with viral vectors. Curr Opin Virol 21, 87–92 (2016). [PubMed: 27591676]
16. Spencer BJ & Verma IM Targeted delivery of proteins across the blood-brain barrier. Proc Natl Acad Sci U S A 104, 7594–7599 (2007). [PubMed: 17463083]
17. Battaglia L & Gallarate M Lipid nanoparticles: state of the art, new preparation methods and challenges in drug delivery. Expert Opin Drug Deliv 9, 497–508 (2012). [PubMed: 22439808]
18. Helm F & Fricker GLiposomal conjugates for drug delivery to the central nervous system. Pharmaceutics 7, 27–42 (2015). [PubMed: 25835091]
19. Kreuter J Drug delivery to the central nervous system by polymeric nanoparticles: what do we know? Adv Drug Deliv Rev 71, 2–14 (2014). [PubMed: 23981489]
20. Mishra B, Patel BB & Tiwari S Colloidal nanocarriers: a review on formulation technology, types and applications toward targeted drug delivery. Nanomedicine 6, 9–24 (2010). [PubMed: 19447208]
21. Papasani MR, Wang G & Hill RA Gold nanoparticles: the importance of physiological principles to devise strategies for targeted drug delivery. Nanomedicine 8, 804–814 (2012). [PubMed: 22306155]
22. Clark AJ & Davis ME Increased brain uptake of targeted nanoparticles by adding an acid-cleavable linkage between transferrin and the nanoparticle core. Proc Natl Acad Sci U S A 112, 12486–12491 (2015). [PubMed: 26392563]
23. Bharali DJ, et al. Organically modified silica nanoparticles: a nonviral vector for in vivo gene delivery and expression in the brain. Proc Natl Acad Sci U S A 102, 11539–11544 (2005). [PubMed: 16051701]
24. Pardridge WM Drug and gene targeting to the brain with molecular Trojan horses. Nat Rev Drug Discov 1, 131–139 (2002). [PubMed: 12120094]
25. Blanco E, Shen H & Ferrari M Principles of nanoparticle design for overcoming biological barriers to drug delivery. Nat Biotechnol 33, 941–951 (2015). [PubMed: 26348965]
26. Rezvani AR & Maloney DG Rituximab resistance. Best Pract Res Clin Haematol 24, 203–216 (2011). [PubMed: 21658619]
27. Abes R, Gelize E, Fridman WH & Teillaud JL Long-lasting antitumor protection by anti-CD20 antibody through cellular immune response. Blood 116, 926–934 (2010). [PubMed: 20439625]
28. Yan M, et al. A novel intracellular protein delivery platform based on single-protein nanocapsules. Nature Nanotechnology 5, 48–53 (2010).
29. Tian H, et al. Growth-Factor Nanocapsules That Enable Tunable Controlled Release for Bone Regeneration. ACS Nano 10, 7362–7369 (2016). [PubMed: 27227573]
30. Liang S, et al. Phosphorylcholine polymer nanocapsules prolong the circulation time and reduce the immunogenicity of therapeutic proteins. Nano Research 9, 1022–1031 (2016).
31. Zhang L, et al. Prolonging the plasma circulation of proteins by nanoencapsulation with phosphorylcholine-based polymer. Nano Research 9, 2424–2432 (2016).
32. Young G, Bowers R, Hall B & Port M Six month clinical evaluation of a biomimetic hydrogel contact lens. CLAO 23, 226–236 (1997).
33. Chen S, Li L, Zhao C & Zheng J Surface hydration: Principles and applications toward low-fouling/nonfouling biomaterials. Polymer 51, 5283–5293 (2010).

34. Kato Y, et al. Acidic extracellular microenvironment and cancer. Cancer Cell Int 13, 89 (2013). [PubMed: 24004445]
35. Corbet C & Feron O Tumour acidosis: from the passenger to the driver's seat. Nat Rev Cancer 17, 577–593 (2017). [PubMed: 28912578]
36. Ito D, et al. Microglia-specific localisation of a novel calcium binding protein, Iba1. Brain Res Mol Brain Res 57, 1–9 (1998). [PubMed: 9630473]
37. Rosenberg GA, et al. Immunohistochemistry of matrix metalloproteinases in reperfusion injury to rat brain: activation of MMP-9 linked to stromelysin-1 and microglia in cell cultures. Brain Res 893, 104–112 (2001). [PubMed: 11222998]
38. Widney D, et al. Levels of murine, but not human, CXCL13 are greatly elevated in NOD-SCID mice bearing the AIDS-associated Burkitt lymphoma cell line, 2F7. PloS One 8, e72414 (2013). [PubMed: 23936541]
39. Legler DF, et al. B cell-attracting chemokine 1, a human CXC chemokine expressed in lymphoid tissues, selectively attracts B lymphocytes via BLR1/CXCR5. J Exp Med 187, 655–660 (1998). [PubMed: 9463416]
40. Gunn MD, et al. A B-cell-homing chemokine made in lymphoid follicles activates Burkitt's lymphoma receptor-1. Nature 391, 799–803 (1998). [PubMed: 9486651]
41. Charbonneau B, et al. CXCR5 polymorphisms in non-Hodgkin lymphoma risk and prognosis. Cancer Immunol Immunother 62, 1475–1484 (2013). [PubMed: 23812490]
42. Hussain SK, et al. Serum levels of the chemokine CXCL13, genetic variation in CXCL13 and its receptor CXCR5, and HIV-associated non-hodgkin B-cell lymphoma risk. Cancer Epidemiol Biomarkers Prev 22, 295–307 (2013). [PubMed: 23250934]
43. Dobner T, Wolf I, Emrich T & Lipp M Differentiation-specific expression of a novel G protein-coupled receptor from Burkitt's lymphoma. Eur J Immunol 22, 2795–2799 (1992). [PubMed: 1425907]
44. Smith JR, et al. Expression of B-cell-attracting chemokine 1 (CXCL13) by malignant lymphocytes and vascular endothelium in primary central nervous system lymphoma. Blood 101, 815–821 (2003). [PubMed: 12393412]
45. Trentin L, et al. Homeostatic chemokines drive migration of malignant B cells in patients with non-Hodgkin lymphomas. Blood 104, 502–508 (2004). [PubMed: 15001469]
46. Shultz L, et al. Human lymphoid and myeloid cell development in NOD/LtSz-scid IL2R gamma null mice engrafted with mobilized human hemopoietic stem cells. Journal of Immunology 174, 6477–6489 (2005).
47. Chijioke O, et al. Human natural killer cells prevent infectious mononucleosis features by targeting lytic Epstein-Barr virus infection. Cell Rep 5, 1489–1498 (2013). [PubMed: 24360958]
48. Melkus M, et al. Humanized mice mount specific adaptive and innate immune responses to EBV and TSST-1. Nature Med 12, 1316–1322 (2006). [PubMed: 17057712]
49. Shultz LD, Brehm MA, Garcia-Martinez JV & Greiner DL Humanized mice for immune system investigation: progress, promise and challenges. Nat Rev Immunol 12, 786–798 (2012). [PubMed: 23059428]
50. Walsh NC, et al. Humanized Mouse Models of Clinical Disease. Annu Rev Pathol 12, 187–215 (2017). [PubMed: 27959627]
51. Honeycutt JB, et al. Macrophages sustain HIV replication in vivo independently of T cells. J Clin Invest 126, 1353–1366 (2016). [PubMed: 26950420]
52. Wu D, et al. A Bioinspired Platform for Effective Delivery of Protein Therapeutics to the Central Nervous System. Adv Mater, e1807557 (2019).
53. Gasque P, et al. Complement components of the innate immune system in health and disease in the CNS. Immunopharmacology 49, 171–186 (2000). [PubMed: 10904116]
54. Salter MW & Beggs S Sublime microglia: expanding roles for the guardians of the CNS. Cell 158, 15–24 (2014). [PubMed: 24995975]
55. Prinz M & Priller J Microglia and brain macrophages in the molecular age: from origin to neuropsychiatric disease. Nat Rev Neurosci 15, 300–312 (2014). [PubMed: 24713688]

56. Stevens B, et al. The classical complement cascade mediates CNS synapse elimination. Cell 131, 1164–1178 (2007). [PubMed: 18083105]
57. Lin NU, et al. CNS metastases in breast cancer: old challenge, new frontiers. Clin Cancer Res 19, 6404–6418 (2013). [PubMed: 24298071]
58. Zagouri F, et al. Intrathecal administration of trastuzumab for the treatment of meningeal carcinomatosis in HER2-positive metastatic breast cancer: a systematic review and pooled analysis. Breast Cancer Res Treat 139, 13–22 (2013). [PubMed: 23588955]
59. Strayer DS & Kohler H Immune response to phosphorylcholine II, natural “auto”-anti-receptor antibody in neonatal Balb/c mice. Cell Immunol 25, 294–301 (1976). [PubMed: 954109]
60. Su J, et al. Antibodies of IgM subclass to phosphorylcholine and oxidized LDL are protective factors for atherosclerosis in patients with hypertension. Atherosclerosis 188, 160–166 (2006). [PubMed: 16307748]
61. Bertolini F, et al. Endostatin, an antiangiogenic drug, induces tumor stabilization after chemotherapy or anti-CD20 therapy in a NOD/SCID mouse model of human high-grade non-Hodgkin lymphoma. Blood 96, 282–287 (2000). [PubMed: 10891463]
62. Zhen A, et al. Stem-cell Based Engineered Immunity Against HIV Infection in the Humanized Mouse Model. J Vis Exp (2016).
63. Zhen A, et al. HIV-specific immunity derived from chimeric antigen receptor-engineered stem cells. Molecular Therapy 23, 1358–1367 (2015). [PubMed: 26050990]
64. Ringpis G, et al. Engineering HIV-1-resistant T-cells from short-hairpin RNA-expressing hematopoietic stem/progenitor cells in humanized BLT mice. PLoS One 7, e53492 (2012). [PubMed: 23300932]

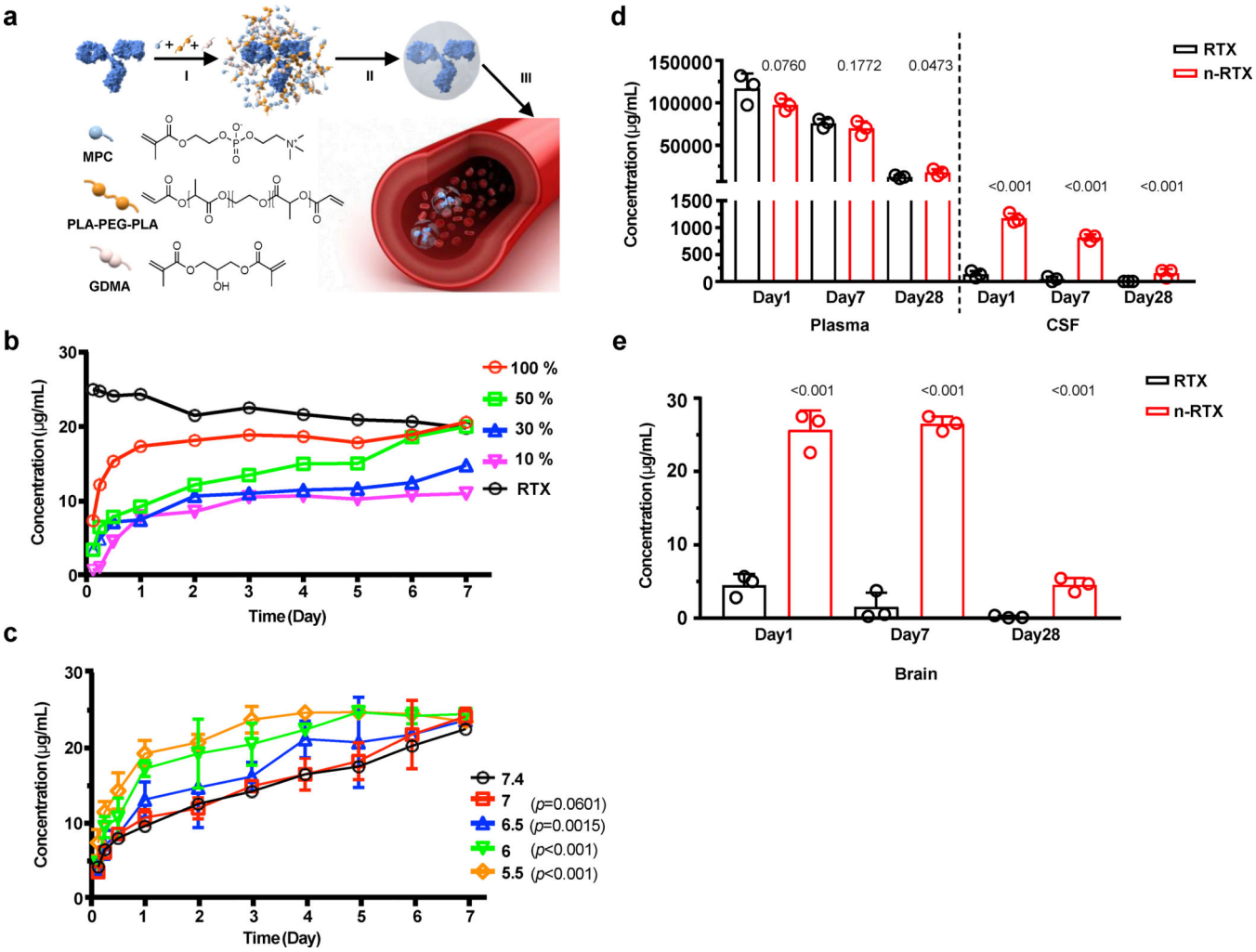

Fig. 1 |. Timed-release nanocapsules facilitate brain delivery of RTX in mice.

a, Scheme of the synthesis and release of timed-release RTX nanocapsules by (**I**) enriching MPC monomer and hydrolysable crosslinker PLA-PEG-PLA and slowly hydrolysable crosslinker GDMA around a RTX molecule, (**II**) *in situ* polymerization of the monomer and crosslinkers forming a thin shell of polymer around a RTX molecule, and (**III**) releasing RTX when polymer shells are degraded under physiological conditions by hydrolysis of the crosslinkers. **b,** RTX nanocapsules were synthesized with mixed crosslinkers GDMA and PLA-PEG-PLA, at which the ratios of PLA-PEG-PLA were 100%, 50%, 30%, and 10%. Twenty-five μg of each nanoencapsulated RTX or native RTX (RTX) was added into 1mL of PBS and incubated at 37 °C for 1 week. The concentration of free RTX was measured by ELISA. **c,** The release rates of RTX nanocapsules with 50% PLA-PEG-PLA crosslinkers were compared in PBS buffers with various pH values presenting physiological conditions (pH=7.4 and 7) and acidic pH conditions (pH=6.5, 6, and 5.5). Twenty-five μg of each sample were added into 1mL of PBS buffer and incubated at 37 °C for up to 1 week. The concentration of free RTX was measured by ELISA. Data are shown as means ± standard deviations (SDs) of biological duplicates. The statistical significance of the pH7.4 (physiological condition) was assessed by *p*-value, calculated by one-tailed paired *t*-test with

Welch's correction. **d,e,** B6 mice (n=3) were administrated with 20 mg/kg of native RTX or RTX nanocapsules with 50% PLA-PEG-PLA crosslinkers (n-RTX) via retro-orbital vein. Plasma, CSF (**b**), and perfused brain tissue samples (**c**) were collected and concentrations of free RTX were measured by ELISA on days 1, 7, and 28. Data are shown as means ± SDs of biological triplicates. The statistical significance of the data for the native RTX group was assessed via *p*-values (provided), calculated by one-tailed unpaired *t*-test with Welch's correction.

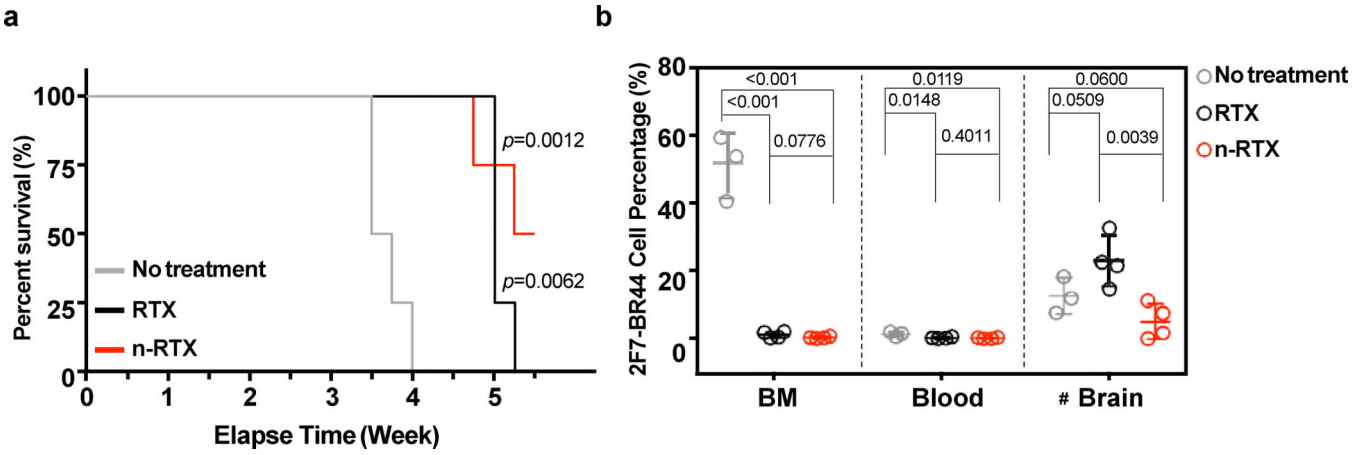

Fig. 2 |. Nanocapsulation enhances anti-lymphoma activity of RTX against CNS lymphomas in the 2F7-BR44 murine xenograft model.

2F7-BR44 cells (2×10^6/animal) in 100 μL Hank's balanced salt solution were injected into NSG mice via tail vein. Five days after injection, mice were randomly separated into three groups: no treatment (n=3), native RTX and n-RTX treatment (n=4). Native RTX or n-RTX was injected via retro-orbital vein at 4 mg/kg/day for 5 days. **a,** Kaplan-Meier survival curves of the mice in each group were plotted relative to the number of weeks after 2F7-BR44 cell injection. The statistical significance was shown with a *p*-value calculated by the log-rank test. **b,** Tissue distribution of 2F7-BR44 cells in blood, perfused bone marrow (BM) and brain was analyzed by flow cytometry at endpoints. Data are shown means ± SDs of biological triplicates (No treatment) or quadruplicates (RTX or n-RTX). Statistical significance was calculated with respect to the no treatment group using a *p*-value calculated by one-tailed unpaired *t*-test with Welch's correction. #: Note that the apparent higher tumor burden in brain of the native RTX group compared to the no-treatment group is due to one-week longer duration of the native RTX group versus the no-treatment group which were euthanized one week earlier due to massive systemic tumor growth.

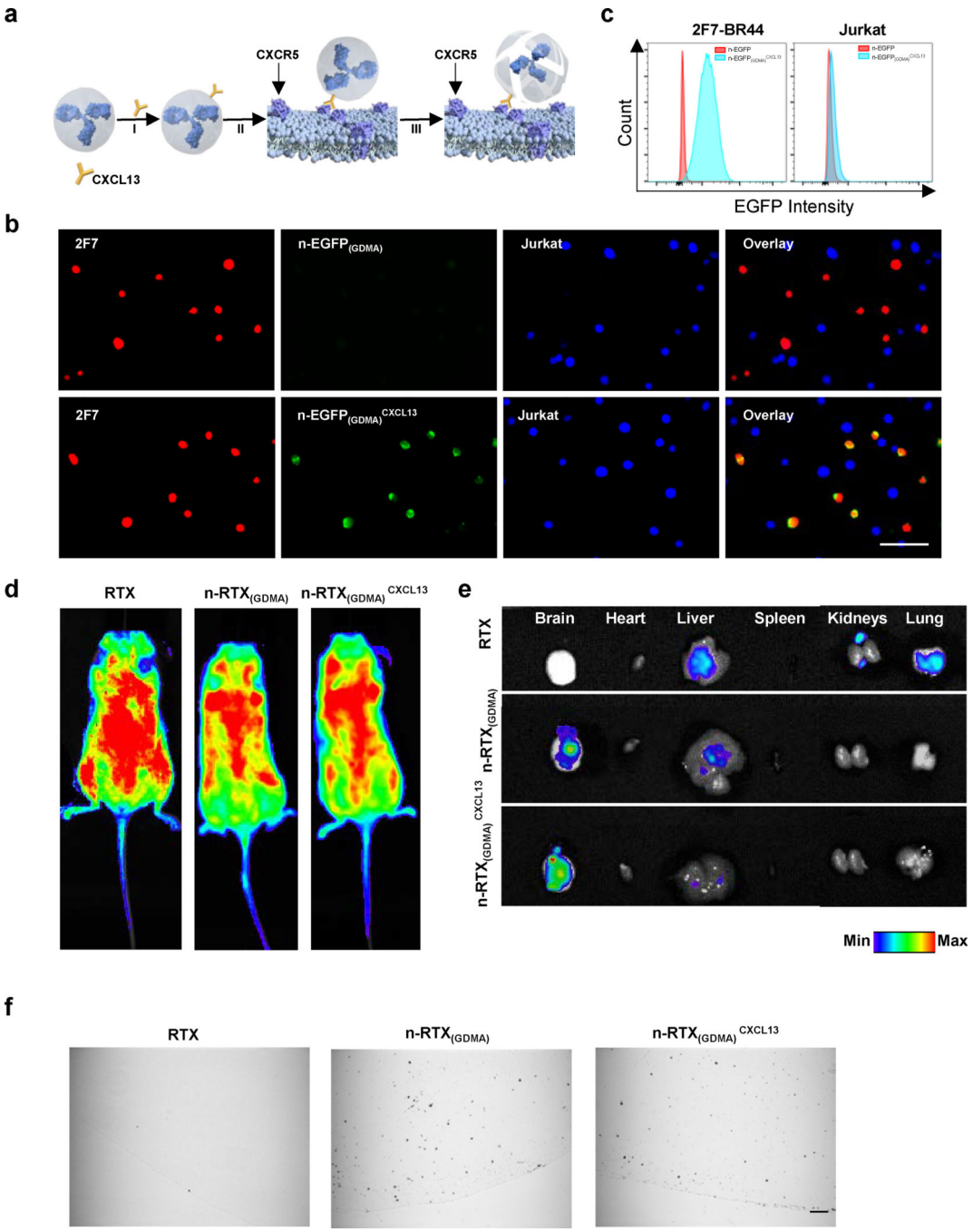

Fig. 3 |. CXCL13 conjugation mediates 2F7-BR44 cell specific nanocapsule targeting without affecting overall biodistribution.

a, Scheme of CXCL13 conjugation on n-RTX$_{(GDMA)}$. CXCL13 was conjugated to n-RTX$_{(GDMA)}$ at a molar ratio of 1:1 through copper-free click chemistry. **b,c,** EGFP nanocapsules with 100% slowly hydrolysable crosslinkers, GDMA, (n-EGFP$_{(GDMA)}$) conjugated with or without CXCL13 (0.1 mg/ml each) were incubated 1 hour at 37^{O}C with a mixed cell population of 2F7-BR44 cells (2F7, mStrawberry+) and Jurkat T cells (Jurkat, BFP+). The binding of each nanocapsule on each cell population was analyzed on Leica

DMi8 inverted microscope (**b**) or on BD LSRFortessa (**c**). The same experiments were repeated independently three times. **d,e,** NSG mice (n=3) were administrated with 20 mg/kg of carboxytetramethylrhodamine (TAMRA)-labelled RTX, n-$RTX_{(GDMA)}$ and n-$RTX_{(GDMA)}^{CXCL13}$ via tail vein. Fluorescence images of whole body (**d**) and each organ (**e**) were taken 1 day after administration. **f,** NSG mice (n=3) were administrated with 20 mg/kg of gold-nanoparticle labelled RTX, n-$RTX_{(GDMA)}$ and n-$RTX_{(GDMA)}^{CXCL13}$ via tail vein. Brain tissues were obtained 1 day after administration and processed for immunohistochemical analysis. Gold nanoparticles in paraffin sections were analyzed following silver enhancement, in which present as black depositions. Bar=50 μm.

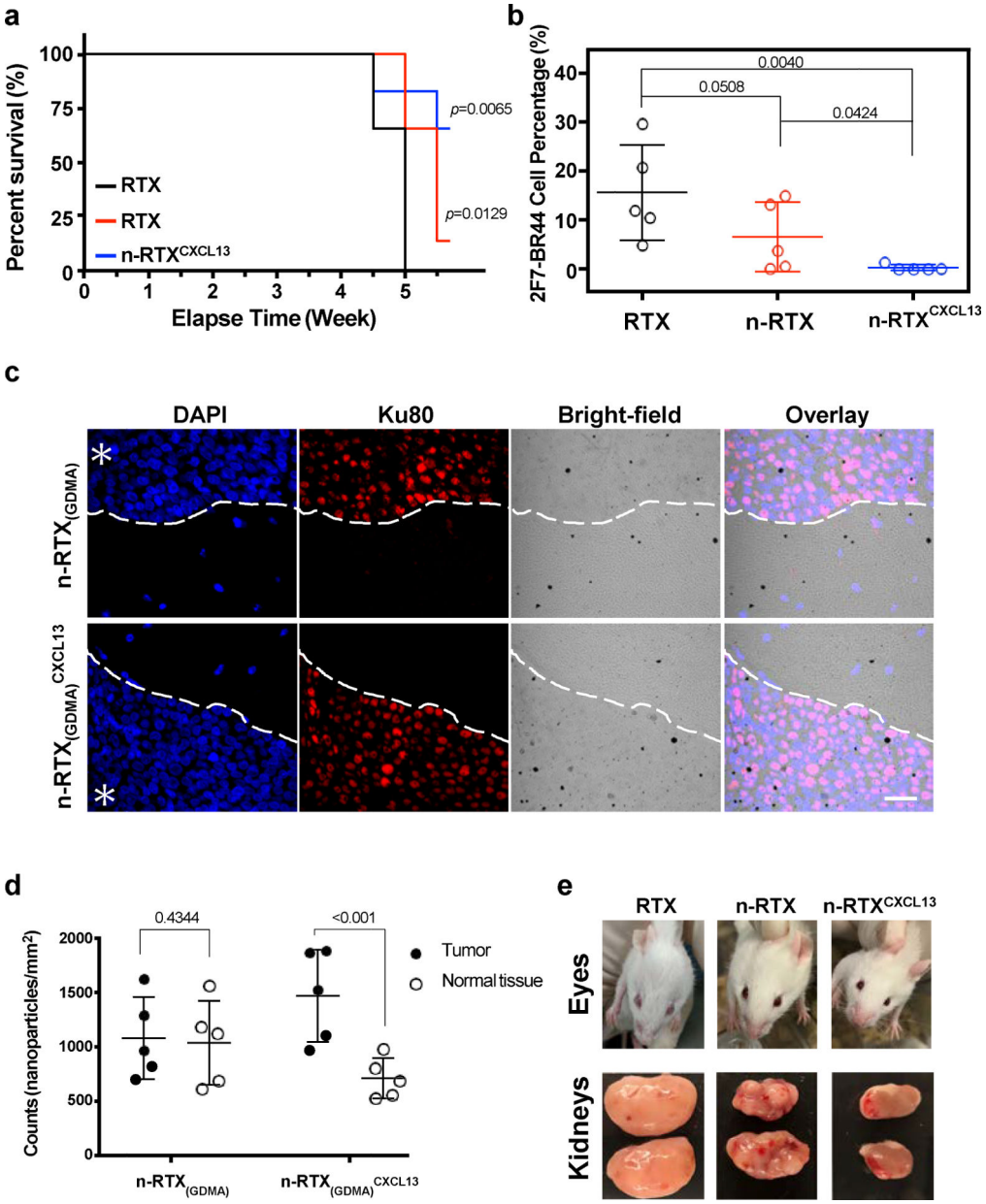

Fig. 4 |. CXCL13 conjugation improves anti-lymphoma activity of n-RTX.

a,b, 2F7-BR44 cells were injected to NSG mice via tail vein (2×10^6/animal). Five days after the injection, mice were randomly separated into three groups (n=5): native RTX, n-RTX, and n-RTX^{CXCL13}. Each form of RTX was administrated via retro-orbital injection at 4mg/kg/day for 5 days. Kaplan-Meier survival curves of the mice in each group were plotted relative to the number of weeks after 2F7-BR44 cell injection (**a**). Statistical significance was shown with a *p*-value calculated by the log-rank test. Percentages of 2F7-BR44 cells in the brain were analyzed by flow cytometry at endpoints following cardiac perfusion (**b**). The statistical significance was calculated to the native RTX group using a *p*-value calculated by one-tailed unpaired *t*-test with Welch's correction. Data are shown means ± SDs of biological quintuplicates. **c,d,** Localizations of gold-labelled n-RTX$_{(GDMA)}$ with or without

CXCL13 conjugation were analyzed in the brain of 2F7-BR44 xenograft NSG mice (n=3) 3 weeks after xenograft. One day after administration of gold-labelled n-$RTX_{(GDMA)}$ or n-$RTX_{(GDMA)}^{CXCL13}$ via retro-orbital injection, brain tissue samples were processed for immunohistochemical analysis (**c**). Gold nanoparticles in paraffin sections were analyzed following silver enhancement, presented as black depositions. 2F7-BR44 cells were stained with anti-human Ku80 antibody and rhodamine red-X anti-rabbit IgG. The nuclei were stained by 4′,6-diamidino-2-phenylindole (DAPI). Asterisks indicate the tumor site while the white dash curves illustrate the boundary of tumor-normal parenchyma. Bar=25 μm. The average counts of gold-labelled n-$RTX_{(GDMA)}$ or n-$RTX_{(GDMA)}^{CXCL13}$ per mm^2 from 5 spots in representatives in Fig.4C (total counts from samples administrated with n-$RTX_{(GDMA)}$ or n-$RTX_{(GDMA)}^{CXCL13}$ are approximately 11,000, respectively) in both the tumor site and normal tissue site were quantified by ImageJ (**d**). The statistical significance was calculated to normal tissue using a *p*-value calculated by one-tailed unpaired *t*-test with Welch's correction. **e,** Representative images of intraocular lymphoma and lymphoma surrounding the kidney in each group.

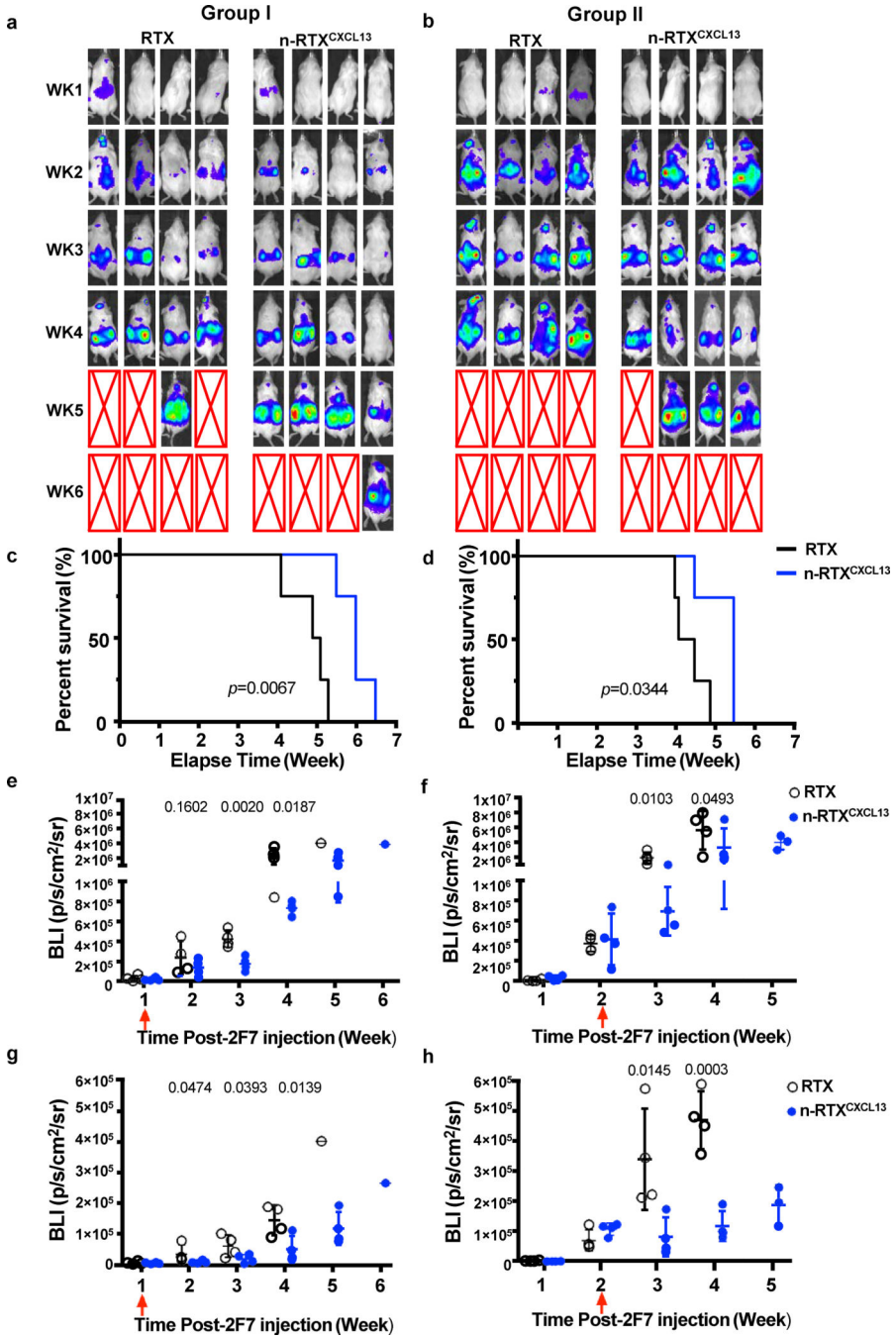

Fig. 5 |. CXCL13 conjugation improves anti-lymphoma activity of n-RTX at different stages of lymphoma progression.

CXCL13 was conjugated to n-RTX at a molar ratio of 1:1 through copper-free click chemistry (n-RTX^{CXCL13}). 2F7-BR44 cells expressing firefly luciferase (2F7-BR44-Luc) were injected to NSG mice via tail vein (2×10^6/animal) (**a-h**). Mice were randomly separated into four groups (n=4): native RTX or n-RTX^{CXCL13} treatment at week 1 (**a,c,e,g,** Group I) or week 2 (**b,d,f,h,** Group II) after 2F7-BR44-Luc cell injection. Each form of RTX was injected via retro-orbital vein at 4 mg/kg/day for 5 days. **a,b,** The tumor progression and

metastasis status were monitored weekly by using bioluminescence imaging on IVIS Lumina II In Vivo Imaging system. Red arrows show the treatment time in each figure. Expansion and metastasis status of 2F7-BR44-Luc cells in NSG mice treated with native RTX or n-RTX^{CXCL13} at week 1 (Group I) or week 2 (Group II) as visualized by bioluminescence imaging. The red X boxes represent deceased mice. Sensitivity settings were adjusted at each time point to maintain 500–5000 counts per pixel and assigned the same color scale for both groups. **c,d,** Kaplan-Meier survival curves of the mice in each group were plotted relative to the number of weeks after 2F7-BR44-Luc cell injection. **e,f,** The bioluminescence intensity (BLI) in the whole body was compared between mice with treatment by native RTX and n-RTX^{CXCL13} in both groups and expressed in photons per second per square centimeter per steradian (p/s/cm^2/sr). **g,h,** The BLI from head area was compared between mice with treatment by native RTX and n-RTX^{CXCL13} in both groups. Data are shown means ± SDs of biological quadruplicates. Statistical significance based on the native RTX group using a *p*-value was calculated by one-tailed unpaired *t*-test with Welch's correction.

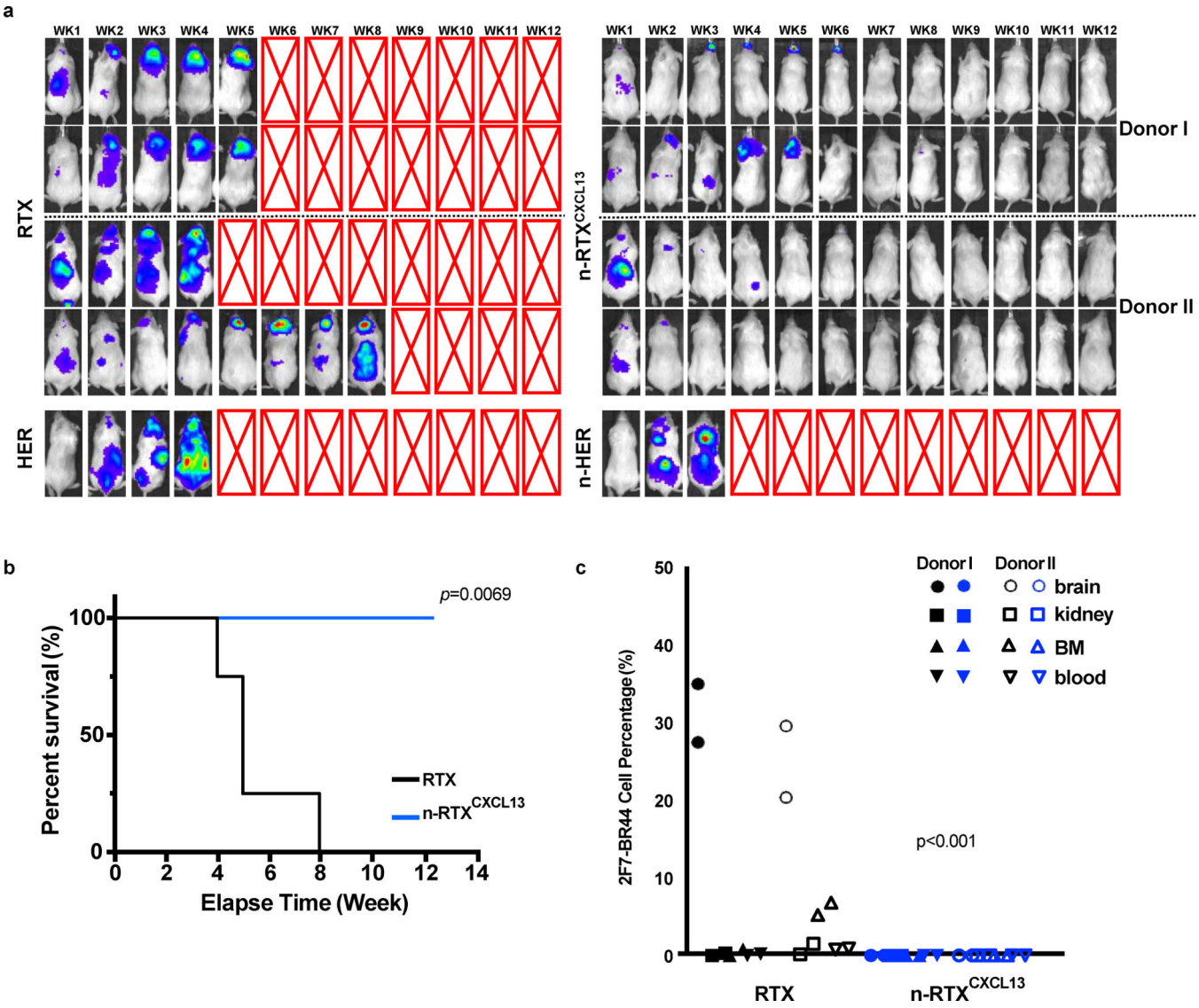

Fig. 6 |. n-RTX^{CXCL13} exhibits superior anti-lymphoma activity against CNS lymphomas in the 2F7-BR44-Luc cell xenograft humanized mice.

2F7-BR44-Luc cells (2×10^6/animal) were injected into humanized BLT mice generated from two independent donors (Donors I and II) via tail vein (**a-c**). Mice were randomly separated into two groups for treatment by native RTX or n-RTX^{CXCL13} at week 1 after the injection. Each form of RTX was administrated via retro-orbital vein at 4 mg/kg/day for 5 days. The tumor progression status was tracked weekly using bioluminescence imaging on IVIS Lumina II In Vivo Imaging system. **a,** Biodistribution of 2F7-BR44-Luc cells in humanized mice treated with native RTX or n-RTX^{CXCL13} at week 1 as visualized by luciferase bioimaging. The red X boxes represent deceased mice. Sensitivity settings were adjusted at each time point to maintain 250–5000 counts per pixel and assigned the same color scale for all treatment groups. **b,** Kaplan-Meier survival curves of the mice were plotted relative to the number of weeks after injection. Necropsies were performed at the end of the experiment (week 13). The statistical significance was shown with a *p*-value calculated by the log-rank

test. **c,** Percentages of 2F7-BR44-Luc cells in tissues were assessed by flow cytometry following cardiac perfusion at the endpoints. HER: naive Herceptin. n-HER: Herceptin nanocapsule. The statistical significance was calculated for all tissues from the native RTX group using a *p*-value, calculated by one-tailed unpaired *t*-test with Welch's correction.